BIOPHYSICS
AND MEDICAL PHYSICS

Analysis of Radiation Shielding Characteristics of Magnetite/High Density Polyethylene Nanocomposite at Diagnostic Level Using the MCNPX, XCOM, XMuDat and Auto-Zeff Programs

M. A. Hosseini[a], S. Malekie[b,*], and M. Keshavarzi[c]

[a] *Ionizing and Non-Ionizing Radiation Protection Research Center (INIRPRC), School of Paramedical Sciences, Shiraz University of Medical Sciences, Shiraz, Iran*

[b] *Radiation Application Research School, Nuclear Science and Technology Research Institute, PO Box 31485-498, Karaj, Iran*

[c] *Department of Nuclear Engineering, Islamic Azad University, Arsanjan Branch, Arsanjan, Iran*

*e-mail: smaleki@aeoi.org.ir

Abstract—Given the lack of data on radiation shielding properties of ironoxide (magnetite) against gamma-rays, this study addresses radiation shielding characteristics of a novel lead-free material, namely magnetite/high density polyethylene ($HDPE/Fe_3O_4$) nanocomposite for diagnostic radiology and nuclear medicine purposes.Thus, radiation shielding characteristics of this nanocomposite, including mass attenuation coefficients, half-value layer (HVL) and transmittance (I/I0%) valuesat various concentrationsnamely 0, 1.16, 1.93, 3.87, 5.8, and 7.74 wt % were obtained viathe MCNPX code at low and medium energies. The simulation simulation results exhibited a good agreementwith the other approaches namely XCOM and XMuDat programs. Besides, the effective atomic number was calculated using direct-method and Auto-Zeff software. The results showed that with an increase in the magnetite wt %, the mass attenuation coefficients underwent an increasing trend followed by the effective atomic number.

1. INTRODUCTION

Iron and its alloys are important elements with many applications in various industries. Magnetite (Fe_3O_4) and hematite (Fe_2O_3) are two known chemical forms of iron that can be synthesized in very small physical dimensions (micro and nanometers) via different methods. Their high biocompatibility and their ability to be synthesized in the mentioneddimensions have led to a unique form of iron [1−4].

Magnetite displays high superparamagnetic properties as well as specific electrical conductivity in nanometer dimensions (<100 nm) [1, 3−5]. Thus, magnetiteor its compounds have received serious attention as contrast agents in MRI imaging to replace conventional materials [6−8]. Accordingly, the effective use of magnetite compounds in dyeing, photocatalysis, drug delivery, magnetic field maintenance, cancer treatment by hyperthermia [8−10], and the study of nanocomposites for electromagnetic shields account for the growing interest in this material [11, 12].

In addition to the unique properties detailed above, iron nanoparticles can be used to design radiation protection nanocomposites due to their several advantages: First, iron shows absorption and attenuation properties against photon radiation from X and gamma rays. For example, at low energy levels (≈ 7 keV), due to significant increases in the probability of photoelectric interaction, radiation absorption rate can increase greatly [13]. Besides, iron has a lower atomic number ($Z = 26$) than conventional materials such as lead and bismuth. Although the low radiation absorption efficiency may be considered a defect at first glance, reducing the secondary radiation due to lower atomic numbers can be considered an advantage for shielding materials such as markers and protective materials for sensitive organs. These materials are often located near the body to reduce exposure during diagnostic processes [14−17]. As a low-Z adsorbent, iron is expected to be effective in other respects as well. Since the use of low-Z adsorbents (such as aluminum) has already been proven effective in diagnostic radiology and the presence of low-energy photon sources

Table 1. The weight fraction values of the elements and total density (gr/cm^3) for the six samples based on the initial data

Sample	Contents (% Fe$_3$O$_4$)	H	C	O	Fe	ρ_{total}, g/cm^3
1	0 (raw HDPE)	0.144	0.856	0	0	0.952
2	1.160	0.142	0.847	0.003	0.008	0.961
3	1.930	0.141	0.840	0.005	0.014	0.967
4	3.870	0.138	0.823	0.011	0.028	0.983
5	5.80	0.135	0.807	0.016	0.042	0.999
6	7.740	0.133	0.790	0.021	0.056	1.009

[18], this class of materials can play a vital role in the design of space shields [19–21]. Thus, despite recent studies on radiation shields produced from materials with high atomic numbers such as lead, bismuth and tungsten [22–24], iron and its compounds are expected to display unique capabilities.

Despite all the benefits detailed above, there seems to be a long way to go before making use of iron composites as X-ray and gamma adsorbents, and previous studies have addressed only a few cases of their applications [25–31].

This being so, the present study focuses on nanocomposites protective properties, including high-density Polyethylene (HDPE) and magnetic nanoparticles (Fe$_3$O$_4$) for protection against X-ray and gamma rays using three MCNPX, XCOM, and XMuDat approaches.

2. MATERIALS AND METHODS

2.1. Calculating Mass Attenuation Coefficients

This simulating work was conducted to evaluate different aspects of HDPE and Fe$_3$O$_4$ to be used as shielding materials against X-ray and gamma rays. To consider these materials for radiation shielding applications, it is necessary to calculate various parameters, including the mass attenuation coefficient at different energies and the other quantities, including HVL and TVL. High density polyethylene (thereafter called Polyethylene) has desirable mechanical properties, high thermal durability, and the ability to chemically combine with different types of fillers [31, 32]. This polymer with the general (C$_2$H$_4$)-n formula comes in different grades. However, HDPEwith density of 0.985 gr/cm^3 as a relative cheap polymer, is available in large quantities. Magnetite (Fe$_3$O$_4$) can be prepared-with a density of 5.1 gr/cm^3 and average dimensions of 30 nm. This study focused on six compounds with different weight fractions of Fe$_3$O$_4$ including raw polyethylene (0 w/w% Fe$_3$O$_4$), 1.2%, 1.93%, 3.9%, 5.8%, and 7.8% Fe$_3$O$_4$. The reason for using these values for the samples can be justified according to the other investigations in the literature considering the probability of occurring agglomeration effect for the poly-

mer nanocomposites filled with nanoparticles above $\approx$10 wt % [33–35]. Table 1 presents more details about the properties of the samples.

MCNPX 2.6 Code with remarkable particle transport simulation capability was used to investigate the attenuation/absorption properties of the samples. First, a validated narrow beam configuration (Fig. 1) was used. Cesium Iodide (CsI) material with a density of 4.51 gr/cm^3 was defined as the detector in Cell 1. The source in the code was defined as an anisotropic and collimated point with a lead chamber and aperture (Cell 2) that, like a gamma source (NPS = 1E+7), produced and emitted particles into the simulation medium. Each time the program was run, single energy photons with energies of 15, 59, 122, 356, 511, and 511 keV were considered low and medium energy particles. In the program, F4 tally was used to calculate the volume flux of the particles in the detector as photon radiation intensity. Here, the air (green color) was considered inside cell 4, and was assumed to be void out side the universe. The energy cut-off in the program was also equal to 1 keV.

The linear attenuation coefficients of each compound were calculated at a given energy level using the following Beer-Lambert formula [36, 37]:

$$\mu = \frac{\ln(I/I_0)}{x}, \qquad (1)$$

where I_0 and I are the F4 tally outputs calculated at the termination of each run in the absence and presence of the shielding materialrespectively, and x is the thickness of the target under analysis. In this study, the linear fitted curve (Fig. 2) was used to calculate the linear attenuation coefficients.

After calculating μ, the HVL can be measured using the following equation:

$$HVL = \ln 2/\mu. \qquad (2)$$

The mass attenuation coefficient, calculated as the linear attenuation coefficient divided by density (μ/ρ), and the I/I_0 value as a transmittance factor [37] were used for the analysis of the attenuation and absorption behaviors of the nanocomposites.

In addition to the above equations, the mass attenuation coefficients were calculated via two other methods. In the first method, through online access and definition of the mentioned compounds using XCOM [38], the attenuation coefficient values of the elements ($Z = 1-92$) were tabulated by Hall et al. (1992) [39]. Besides, in the third method, XMuDat software was used based on the data tabulated by Boone et al. (1998) [40].

2.2. Calculating the Effective Atomic Number

When analyzing the attenuation rate of photons in a substance, the effective atomic number (Z_{eff}) and its behavior play an important role in determining the absorption and attenuation of radiations [41].

There are several ways to calculate the effective atomic number (Z_{eff}). For example, in the comparative method, this quantity is defined as follows:

$$Z_{eff} = \frac{\sigma_a}{\sigma_e}, \tag{3}$$

where σ_a and σ_e are atomic and electronic cross-sections respectively and are defined via the following equations for a composite consisting of different elements:

$$\sigma_a = \frac{\sigma_m}{\sum_i n_i}, \tag{4}$$

$$\sigma_e = \frac{1}{N_A} \sum_i \frac{f_i A_i}{Z_i} \left(\frac{\mu}{\rho}\right) i, \tag{5}$$

where N_A is the Avogadro number, A_i and Z_i are the atomic mass and the atomic number of element i, n_i is the number of atoms in the molecule, and f_i is the atomic fraction of the element in the composite.

Besides, σ_m in Eq. (4) estimates the effective molecular cross-section and is related to the total mass attenuation coefficient (μ/ρ) through the following equation [41, 42]:

$$Q_m = \frac{\left(\frac{\mu}{\rho}\right)\left(\sum_i n_i A_i\right)}{N}. \tag{6}$$

Finally, the effective atomic number in the interaction of photons with the composite can be directly calculated by the following practical formula:

$$Z_{eff} = \frac{\sum_i f_i A_i \left(\frac{\mu}{\rho}\right)_i}{\sum_j f_j \frac{A_j}{Z_j}\left(\frac{\mu}{\rho}\right)_j}, \tag{7}$$
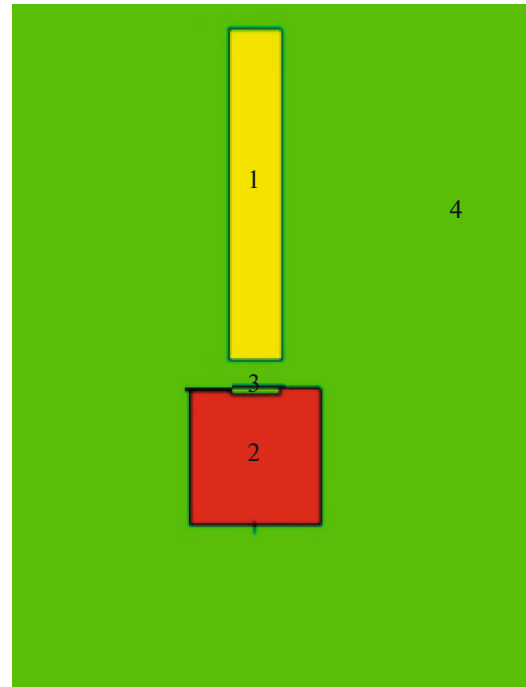

Fig. 1. The designed geometry layout of the narrow beam in MCNPX code, including CsI detector (cell 1), a lead collimator (cell 2), and the target (cell 3) with a point source surrounded by the collimator, and the environment (cell 4).
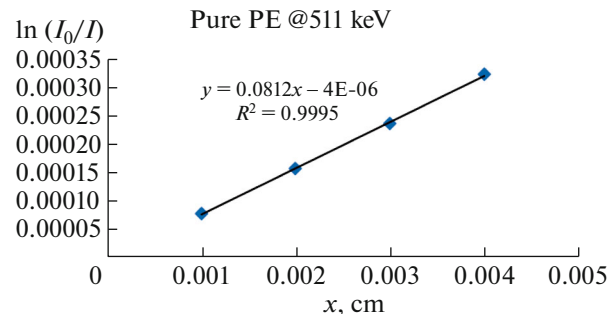

Fig. 2. A linear fitted curve: $\ln(I_0/I)$ values in different thicknesses (x) for raw Polyethylene. The calculated slope (corresponding to the linear attenuation coefficient) and the degree of linearity (R^2) are shown in the curve.

here, A_i and Z_j are the atomic weight and atomic number, respectively, and $\left(\frac{\mu}{\rho}\right)_i$ is the total mass attenuation coefficient for the element, which varies depending on the photon energy. Further details about this method can be found in [43, 44].

In the present study, the effective atomic number values for the six composites with the properties listed in Table 1 were calculated by two methods. Eq. (7) was used in the first method to calculate the values, while the mass attenuation and energy absorption coeffi-
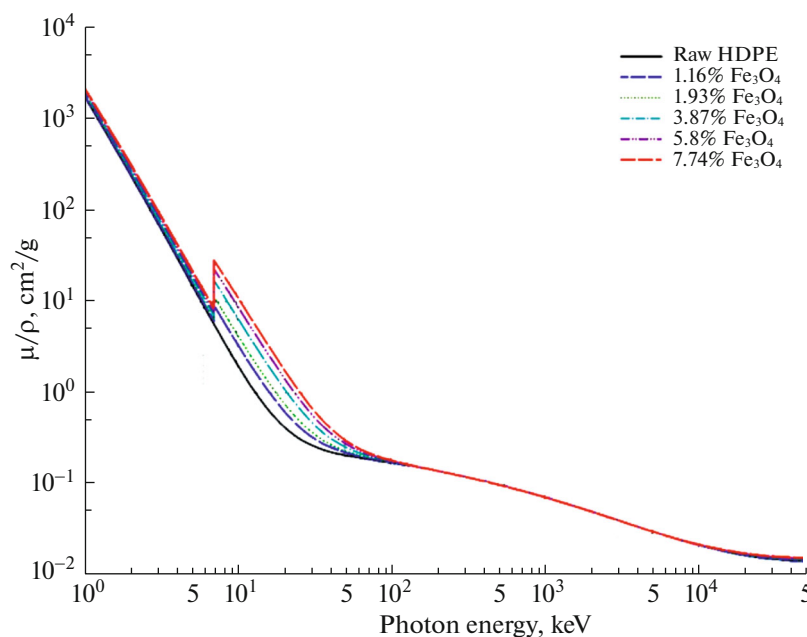
Fig. 3. The approximate values of mass attenuation coefficients versus photon energy: The absorption half-value layers in the Iron-containing composites ($E \sim 7$ keV) are also shown for the samples understudy.

cients were extracted from the data proposed by Boone et al. [40]. In the other method, the Auto-Zeff software was used to calculate the mentioned coefficients. It should be noted that extensive energy sources can be defined as single and multiple energies in this software. In addition to the possibility of defining materials and compounds (based on user needs), some well-known important compounds such as bone, some widely used polymers, etc., are defined by default based on the software standards [45].

3. RESULTS

3.1. The Mass Attenuation Coefficients and Effective Atomic Number in the Composites

Figure 3 presents the approximate values of the total mass attenuation coefficients (taking into account the coherent scattering) for the six selected compounds in the presence of photons at different energy ranges (0.001−50 MeV) using XMuDat software.

As shown in Fig. 3, raw polyethylene displays lower attenuation values compared to other samples at all energies. Besides, absorption/attenuation coefficients undergo significant changesin the energy range of 1−100 keV in other weight percentages, as shown in the curve. Furthermore, an increase in the iron concentration (w/w%) increases the attenuation rate, with sharp peaks revealed in the samples at low energy (~7 keV), which can be attributed to Iron (Fe-26) K-edge absorptions. In general, the data highlight an upward trend in the attenuation coefficients in the samples.

Table 2 shows the values of the total mass attenuation coefficients calculated at the predetermined energy levels (15−511 keV) using the three MCNPX, XMuDat, and XCOM approaches. As can be seen, although there is a good agreement between the calculated values in the three methods, there is a slight difference (up to 15%) between the values obtained using the MCNPX and XMuDat methods. This difference can be attributed to statistical errors in the geometry and calculations performed by Monte Carlo and the cut-off for the photon energy. Furthermore, different values of the mass attenuation coefficients of the elements in the data libraries of the programs can be another reason for this discrepancy. For instance, in composite #6 (containing 7.74% Fe_3O_4), there is a difference in the second digit after the decimal point (3.933 vs. 3.924 cm^2/g) in the attenuation coefficients at the energy level of 15 keV energy calculated using XCOM and XMuDat. However, as the energy increases, this difference becomes almost negligible.

The changing trend of the mass attenuation coefficients shown in Fig. 3 can be explained by looking at the effective atomic numbers curves (Fig. 4). As can be seen, the effective atomic numbers have changed significantly at energies less than 100 keV. For instance, the effective atomic number has reached its maximum at the energy level of ~7 keV, undergoing a downward trend afterward.However, no significant difference is remarked at the energy level above 100 keV.

Besides, the corresponding values calculated using the two methods show some differences. However, this difference is slightly more noticeable at low ener-

Table 2. The total mass attenuation coefficients estimated at five energy levels for the studied composites using three different methods

E, keV	μ/ρ (cm²/g) by MCNP					μ/ρ (cm²/g) by XMuDat					μ/ρ (cm²/g) by XCOM				
	15	59	122	356	511	15	59	122	356	511	15	59	122	356	511
#1	0.681	0.191	0.133	0.096	0.085	0.748	0.198	0.163	0.114	0.098	0.746	0.198	0.163	0.114	0.099
#2	1.151	0.174	0.134	0.098	0.086	1.226	0.207	0.163	0.114	0.098	1.222	0.207	0.164	0.114	0.098
#3	1.460	0.211	0.134	0.098	0.085	1.542	0.212	0.164	0.113	0.098	1.538	0.213	0.164	0.114	0.098
#4	2.247	0.190	0.135	0.098	0.086	2.341	0.227	0.165	0.113	0.098	2.335	0.228	0.166	0.114	0.098
#5	3.038	0.205	0.138	0.098	0.084	3.135	0.242	0.167	0.113	0.098	3.127	0.242	0.167	0.113	0.098
#6	3.837	0.218	0.139	0.084	0.083	3.933	0.257	0.168	0.098	0.097	3.924	0.257	0.168	0.098	0.097

gies (<100 keV), which can be attributed to the differences in the attenuation coefficients of the elements at low energies, as evident in other studies [41, 42].

3.2. Half-Value Layer (HVL) Values of the Nanocomposites

The curves in Figs. 5a–5e show the HVL values for each nanocomposite at different energy levels. As expected, at very low energies (15 keV), only a few millimeters (maximum 1 cm) are necessary to halve the radiation intensity. This trend also improved as the weight percentage of Iron increased. For instance, at the highest concentration (7.74%), only 0.18 cm is needed to halve the radiation intensity, as was confirmed by the results obtained via the three methods. However, HVL values continue to increase at higher energies. Depending on the Iron oxide concentration in the samples, the thickness required to halve the radiation intensity is estimated as 2–4 cm at 59 keV,

4.5–5 cm at 122 keV, 6–7.5 cm at 356 keV, and finally 7–8.5 cm at 511 keV (see Fig. 5 for more details).

3.3. The Transmittance Values in the Nanocomposites

To evaluate the attenuation/absorption behavior of the samples as markers with potential applications in radiology and nuclear medicine, the I/I_0 % curve can be examined [29], as shown in Fig. 6.

It should be noted that radiology markers, depending on the amount of radiation passing through the material, fall under the two categories of radiopaque (~100% absorption and close to zero percent transmittance) or radiolucent (transmitting a higher percentage of radiation) [46].

Figures 6a–6e show the mean transmittance values for the six nanocomposites with thicknesses of 0.1 to 5 cm at different photon energies. As shown in Fig. 6a, the nanocomposites display good radiolucent properties at the lowest energy (15 keV). In other words, the first step of increasing the magnetite con-
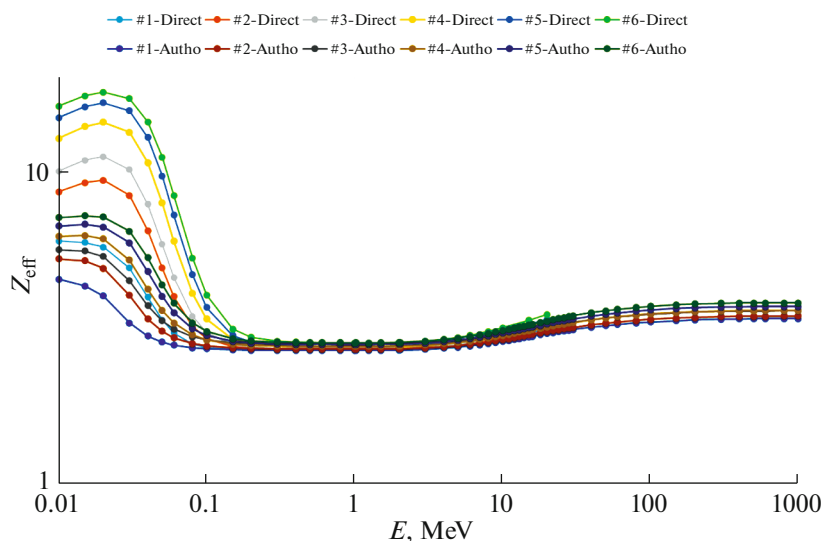

Fig. 4. The effective atomic number changes for the six composites under study at different energies by the two direct and Auto-Zeff methods.

HVL (cm) 15 keV (a)

■ MCNPX ■ XMuDat ■ XCOM

	#1	#2	#3	#4	#5	#6
MCNPX	1.07	0.63	0.49	0.31	0.23	0.18
XMuDat	0.97	0.59	0.46	0.30	0.22	0.17
XCOM	0.98	0.59	0.47	0.30	0.22	0.18

HVL (cm) 59 keV (b)

■ MCNPX ■ XMuDat ■ XCOM

	#1	#2	#3	#4	#5	#6
MCNPX	3.81	4.18	3.39	3.72	3.39	3.14
XMuDat	3.68	3.49	3.37	3.10	2.87	2.68
XCOM	3.68	3.49	3.37	3.10	2.86	2.67

HVL (cm) 122 keV (c)

■ MCNPX ■ XMuDat ■ XCOM

	#1	#2	#3	#4	#5	#6
MCNPX	5.49	5.39	5.33	5.21	5.03	4.94
XMuDat	4.48	4.41	4.37	4.27	4.16	4.09
XCOM	4.47	4.41	4.37	4.26	4.16	4.09

HVL (cm) 356 keV (d)

■ MCNPX ■ XMuDat ■ XCOM

	#1	#2	#3	#4	#5	#6
MCNPX	7.55	7.35	7.30	7.18	7.09	7.04
XMuDat	6.41	6.35	6.32	6.23	6.15	6.10
XCOM	6.39	6.33	6.30	6.21	6.13	6.08

HVL (cm) 511 keV (e)

■ MCNPX ■ XMuDat ■ XCOM

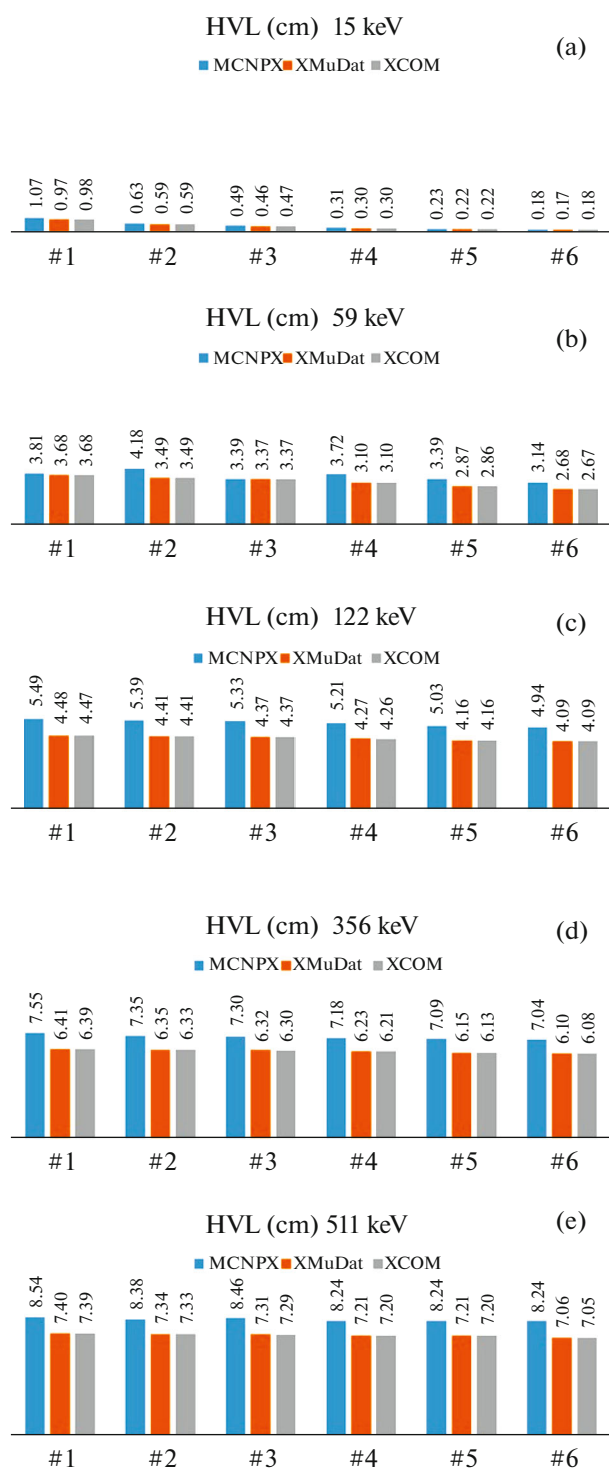|	#1	#2	#3	#4	#5	#6
MCNPX	8.54	8.38	8.46	8.24	8.24	8.24
XMuDat	7.40	7.34	7.31	7.21	7.21	7.06
XCOM	7.39	7.33	7.29	7.20	7.20	7.05

Fig. 5. Estimating theHVL values at different energies including (a) 15, (b) 59, (c) 122, (d) 356, and (e) 511 keV using three different approaches

centration (1.16%) led to the crude polymer displaying radiation absorption of close to 100% at a thickness of 3 cm. However, as the concentration increases, the thickness decreases so that at its maximum concentration, the magnetite materials should be 1 cm thick for

almost complete absorption of photon radiation at this energy level.

Besides, as the energy increases to 59 keV (Fig. 6b), the nanocomposites started to display radiolucent properties, so that the transmittance rate varies from 30% to 90% at the minimum and maximum thicknesses. It should be noted that as the concentration of the filler increases, the radiation absorption at this energy level is still considerable. However, with increasing energy (Figs. 6c–6e), this advantage disappears and becomes almost imperceptible. For example, the transmittance rate of the all samples was examined at 511 keV, as shown in Fig. 6e. As can be seen, all the samples have shown almost the same behavior at this energy level. This trend can, of course, be predicted with the trend observed in Figs. 3 and 5. In other words, Z_{eff} undergoes almost similar changes at this energy level and even higher levels in all six samples. As shown in Fig. 6e, the absorption and transmittance are almost equal (~65%) in all samples at the maximum thickness.

4. DISCUSSION

This study explored the absorption and attenuation properties of six composites with different magnetite and raw polyethylene concentrations at different energy levels using the three MCNPX, XCOM, and XMuDat approaches. The results indicated that the mass attenuation coefficients calculated via the three methods exhibited a good agreement. Nevertheless, the differences at low energy levels were sometimes significant due to the variability of library data. Besides, the attenuation/absorption variations were in good agreement as indicated by the effective atomic numbers (Z_{eff}) calculated using the two methods. The Z_{eff} variations for the six samples showed the attenuation/absorption optimalityat energies less than 100 keV. Moreover, the samples in question exhibited radiopaque properties at 15 keV while these properties tended to become radiolucent at higher energies. Since this energy range is widely used in diagnostic processes such as mammography and general radiography, these composites can also be considered for manufacturing high-performance shields.

A few points deserve serious attention to understand the importance of iron-containing materials as adsorbents in radiology and nuclear medicine. Researchers have shown a growing interest in nanocomposite materials containing iron [25–30] due to their abundance and availability and their high compatibility with the environment [1–4, 9, 10]. However, the use of these materials in radiation science still seems to be in its infancy. As was noted in this study, composites containing iron and raw polyethylene showed the absorption and attenuation capabilities at the low and medium energy ranges. Thus, they are widely used in radiology and diagnostic nuclear med-
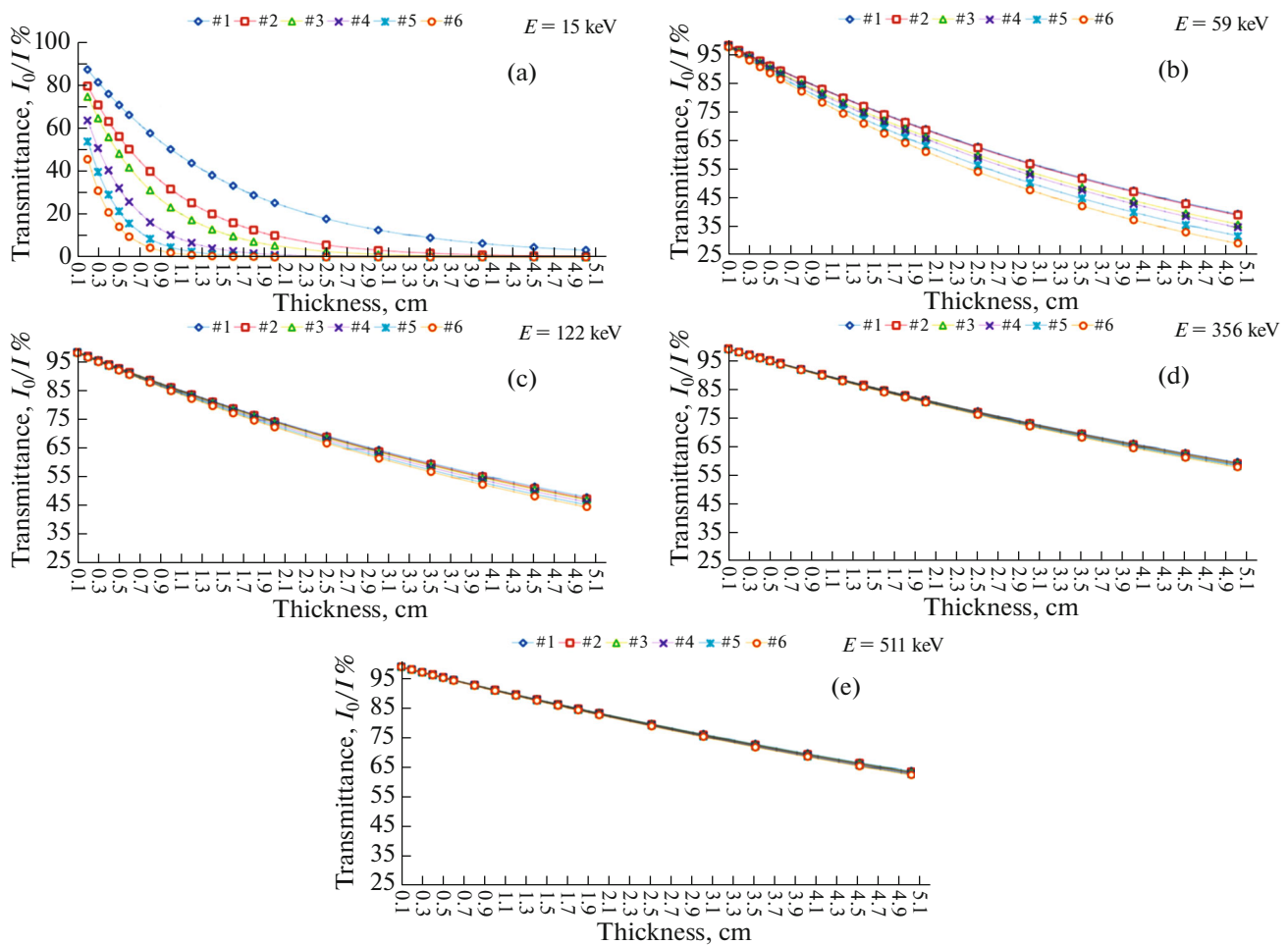
Fig. 6. The transmittance values for the six samples at the photon radiation of (a) 15, (b) 59, (c) 122, (d) 356, and (e) 511 keV.

icine, as highlighted in previous studies [27−30]. Analysis of the attenuation and absorption properties of the nanocomposites revealed the particular shielding characteristics of iron in the presence of photons. Accordingly, since this element has K-edge at the energy level of ~7 keV [13], it can be considered a light and non-toxic protection in low-energy applications (e.g., mammography and general radiology). Besides, in cases where there are no space and cost constraints, these composites can be used at higher photon energies, especially in diagnostic nuclear medicine and CT scans as these materials generate lower secondary radiation and have higher biocompatibility.

The second point to note is the unique properties of Iron in absorbing and attenuating radiation compared to other materials. Since materials such as lead, bismuth, and barium have high atomic numbers, and because of their high efficiency, they have traditionally been used to design shields for use indiagnostic radiology and nuclear medicine [17, 22−24, 36, 37]. However, the formation of secondary radiation (often accompanied by scattered photons) is ignored [14, 15, 17]. In other words, although Iron has a lower effi-

ciency in absorbing radiation than conventional materials due to its low Z, and consequently its lower radiation absorption, it produces less secondary radiation due to its lower atomic number [47]. For example, Iron compounds incorporated into a polymer matrix (with a small atomic number) as radiological markers generate secondary radiation and subsequently reduce the radiation dose, especially in the patient skin. Besides, these compounds play an essential role in maintaining image quality during the imaging procedure.

The last issue of interest is using this composite to protect sensitive organs such as the eyes, thyroid gland, and genitals during diagnostic procedures such as CT scans when the tube current modulation (TCM) has been applied. Several studies have recently shown that the use of high atomic number materials such as bismuth to protect sensitive organs reduces image quality, while a decrease in the unwanted dose was reported [17, 48]. As a result, low-atomic-number materials such as Iron can be considered suitable candidates to replace such materials. Hence, future studies need to further attest the mentioned points.

5. CONCLUSIONS

This study explored the shielding properties of HDPE/Fe$_3$O$_4$ nanocomposite at six different weight percentages of the inclusions namely 0, 1.16, 1.93, 3.87, 5.8, and 7.74 wt % against the photons at low and medium energies using the three MCNPX, XCOM, and XMuDat computational approaches. Depending on the magnetite concentrations, HVL values were estimated as 2−4 cm at 59 keV, 4−5.5 cm at 122 keV, 6−7.5 cm at 356 keV, and 7−8.5 cm at 511 keV energies. Besides, at low energy (e.g., 15 keV), radiopaque properties were observed in all samples, in addition to radiolucent properties displayedat higher energies.

These compounds show radiolucency and radiopaque properties against radiation, depending on the average photon energy and the concentration of Iron oxide in the nanocomposites. Iron, with its low atomic number compared to conventional materials such as bismuth and lead, can produce less secondary radiation while absorbing and attenuating the radiation. This highlights the need for further studies on the applications of iron-containing nanocomposites as skin markers in medical imaging and their use as nontoxic substances to protect sensitive organs during diagnostic processes. Accordingly, it is recommended to conduct further studies on iron-containing nanocomposites.

The data in this study showed that HDPE/Fe$_3$O$_4$ nanocomposite potentially can be used as skin markers with imaging applications and protection of sensitive organs. The superiority of the nanocomposite over high-Z materials can be found in terms of lower secondary radiations generations, taking into account the quality of the images. Thus, these compounds can be considered as X- and gamma-rays shielding materialswith energies lower than 122 keV to be used in diagnostic radiology and nuclear medicine.

CONFLICT OF INTEREST

The authors declare no conflict of interest.

REFERENCES

1. J. Wallyn, N. Anton, and T. F. Vandamme, "Synthesis, principles, and properties of magnetite nanoparticles for in vivo imaging applications—A review," Pharmaceutics **11**, 601 (2019).
https://doi.org/10.3390/pharmaceutics11110601

2. K. K. Kefeni, T. A. Msagati, and B. B. Mamba, "Ferrite nanoparticles: synthesis, characterisation and applications in electronic device," Mater. Sci. Eng. B **215**, 37−55 (2017).
https://doi.org/10.1016/j.mseb.2016.11.002

3. J. Sun, S. Zhou, P. Hou, Y. Yang, J. Weng, X. Li, and M. Li, "Synthesis and characterization of biocompatible Fe3O4 nanoparticles," J. Biomed. Mater. Res. A **80**, 333−41 (2007).
https://doi.org/10.1002/jbm.a.3090917001648

4. S. A. Kulkarni, P. S. Sawadh, P. K. Palei, and K. K. Kokate, "Effect of synthesis route on the structural, optical and magnetic properties of Fe$_3$O$_4$ nanoparticles," Ceram. Int. **40**, 1945−9 (2014).
https://doi.org/10.1016/j.ceramint.2013.07.103

5. B. Liu, N. Wang, J. Jin, H. Liu, and R. Chen, "Photoinduced synthesis of variable-sized magnetite nanoparticles and their photodegradation for orange II," Bull. Mater. Sci. **43** (1), 1−7 (2020).
https://doi.org/10.1007/s12034-020-02137-z

6. N. Arsalani, H. Fattahi, and M. Nazarpoor, "Synthesis and characterization of PVP-functionalized superparamagnetic Fe3O4 nanoparticles as an MRI contrast agent," Express Polym. Lett. **4**, 329−8 (2010).
https://doi.org/10.3144/expresspolymlett.2010.42

7. L. Zareei, B. Divband, A. Mesbahi, M. Khatamian, A. Kiani, and N. Gharehaghaji, "A new potential contrast agent for magnetic resonance imaging: Iron oxide-4A nanocomposite," J. Biomed. Phys. Eng. **9**, 211 (2019).
https://doi.org/10.31661/jbpe.v9i2Apr.75531214526

8. R. C. Popescu, E. Andronescu, and B. S. Vasile, "Recent advances in magnetite nanoparticle functionalization for nanomedicine," Nanomaterials **9**, 1791 (2019).
https://doi.org/10.3390/nano9121791

9. F. Oltolina, A. Peigneux, D. Colangelo, N. Clemente, A. D'Urso, G. Valente, G. R. Iglesias, C. Jiménez-Lopez, and M. Prat, "Biomimetic magnetite nanoparticles as targeted drug nanocarriers and mediators of hyperthermia in an experimental cancer model," Cancers **12**, 2564 (2020).
https://doi.org/10.3390/cancers12092564

10. Y. P. Yew, K. Shameli, M. Miyake, N. B. Khairudin, S. E. Mohamad, T. Naiki, and K. X. Lee, "Green biosynthesis of superparamagnetic magnetite Fe$_3$O$_4$ nanoparticles and biomedical applications in targeted anticancer drug delivery system: A review," Arab. J. Chem. **13**, 2287−308 (2020).
https://doi.org/10.1016/j.arabjc.2018.04.013

11. N. I. Anaraki and R. Poursalehi, "Shielding effectiveness of polymeric nanocomposites filled with iron/wüstite nanoparticles," Proc. Mater. Sci. **11**, 700−5 (2015).
https://doi.org/10.1016/j.mspro.2015.11.041

12. H. Yue, H. Zhang, H. Mao, X. Song, and Z. Ge, "Mechanical property and electromagnetic interference shielding effectiveness of mortar produced with radiation-proof cloths," J. Mater. Civil Eng. **30**, 04018020 (2018).
https://doi.org/10.1061/(ASCE)MT.1943-5533.0002211

13. G. A. Waychunas, M. J. Apted, and G. E. Brown, "X-ray K-edge absorption spectra of Fe minerals and model compounds: Near-edge structure," Phys. Chem. Miner. **10** (1), 1−9 (1983).
https://doi.org/10.1007/BF01204319

14. A. J. Einstein, C. D. Elliston, D. W. Groves, B. Cheng, S. D. Wolff, G. D. Pearson, M. R. Peters, L. L. Johnson, S. Bokhari, G. W. Johnson, and K. Bhatia, "Effect of bismuth breast shielding on radiation dose and image quality in coronary CT angiography," J. Nucl. Cardiol. **19**, 100−8 (2012).
https://doi.org/10.1007/s12350-011-9473-x22068687

15. C. H. McCollough, J. Wang, R. G. Gould, and C. G. Orton, "The use of bismuth breast shields for CT should be discouraged," Med. Phys. **39**, 2321−4 (2012).
https://doi.org/10.1118/1.3681014

16. H. Winter, A. L. Brown, and A. M. Goforth, "Bismuth-based nano- and microparticles in X-ray contrast, radiation therapy, and radiation shielding applications," in *Bismuth: Advanced Applications and Defects Characterization* (InTech Open, Rijeka, 2018), p. 71.
https://doi.org/10.5772/intechopen.76413.

17. P. Mehnati, R. Malekzadeh, and M. Y. Sooteh, "Use of bismuth shield for protection of superficial radiosensitive organs in patients undergoing computed tomography: A literature review and meta-analysis," Radiol. Phys. Technol. **12**, 6−25 (2019).
https://doi.org/10.1007/s12194-019-00500-230790174

18. J. T. Bushberg and J. M. Boone, *The Essential Physics of Medical Imaging* (Lippincott Williams and Wilkins, 2011).

19. P. Senthil Kumar and E. Gunasundari, "Nanocomposites: Recent trends and engineering applications," Nano Hybrids Compos. **20**, 65−80 (2018).
https://doi.10.4028/www.scientific.net/NHC.20.65

20. Z. Zaiemyekeh, G. Liaghat, and M. K. Khan, "Effect of Al_2O_3 nanoparticles on the mechanical behaviour of aluminium-based metal matrix composite synthesized via powder metallurgy," Proc. Inst. Mech. Eng., Part L: J. Mater.: Des. Appl. **235**, 2340−55 (2021).
https://doi.org/10.1177/14644207211033626

21. H. Daneshvar, K. G. Milan, A. Sadr, S. H. Sedighy, S. Malekie, and A. Mosayebi, "Multilayer radiation shield for satellite electronic components protection," Sci. Rep. **11** (1), 1−2 (2021).
https://doi.org/10.1038/s41598-021-99739-2

22. S. A. Hashemi, S. M. Mousavi, R. Faghihi, M. Arjmand, S. Sina, and A. M. Amani, "Lead oxide-decorated graphene oxide/epoxy composite towards X-Ray radiation shielding," Radiat. Phys. Chem. **146**, 77−85 (2018).
https://doi.org/10.1016/j.radphyschem.2018.01.008

23. R. Mehrara, S. Malekie, S. M. Saleh Kotahi, and S. Kashian, "Introducing a novel low energy gamma ray shield utilizing polycarbonate bismuth oxide composite," Sci. Rep. **11**, 10614 (2021). . PMID: .
https://doi.org/10.1038/s41598-021-89773-534011933

24. A. Aghaz, R. Faghihi, S. Mortazavi, A. Haghparast, S. Mehdizadeh, and S. Sina, "Radiation attenuation properties of shields containing micro and nano WO3 in diagnostic X-ray energy range," Int. J. Radiat. Res. **14**, 127 (2016).

25. A. B. Azeez, K. S. Mohammed, A. M. Al Bakri, H. I. Hasan, and O. A. Abdulkareem, "Radiation shielding characteristics of concretes incorporates different particle sizes of various waste materials," Adv. Mater. Res. **925**, 190−194 (2014).
https://doi.org/10.4028/www.scientific.net/AMR.925.190

26. O. Ozyurt, N. Altinsoy, B. Buyuk, and E. Fenerci, "Investigation of shielding performance of concretes produced with iron fillings using betatron X-ray radiography," Acta Phys. Polon. A **129**, 829−31 (2016).
https://doi.org/10.12693/APhysPolA.129.829

27. K. Srinivasan and E. J. Samuel, "Evaluation of radiation shielding properties of the polyvinyl alcohol/iron oxide polymer composite," J. Med. Phys. **42**, 273 (2017). PMID: PMCID: PMC5744457.
https://doi.org/10.4103/jmp.JMP_54_1729296043

28. M. A. Budiawan, S. Suryani, B. Abdullah, and D. Tahir, "Analysis of absorption properties of a composite FlyAsh and Fe_2O_3 for X-ray radiation shielding applications," IOP Conf. Ser.: Mater. Sci. Eng. **593**, 012014 (2019).
https://doi.org/10.1088/1757-899X/593/1/012014

29. M. Lopresti, G. Alberto, S. Cantamessa, G. Cantino, E. Conterosito, L. Palin, and M. Milanesio, "Light weight, easy formable and non-toxic polymer-based composites for hard X-ray shielding: A theoretical and experimental study," Int. J. Mol. Sci. **21**, 833 (2020).
https://doi.org/10.3390/ijms2103083332012889

30. H. O. Tekin, F. Akman, S. A. Issa, M. R. Ka, O. Kilicoglu, and H. Polat, "Two-step investigation on fabrication and characterization of Iron-reinforced novel composite materials for nuclear-radiation shielding applications," J. Phys. Chem Solids **2020**, 109604 (2020).
https://doi.org/10.1016/j.jpcs.2020.109604

31. E. Mansouri, A. Mesbahi, R. Malekzadeh, and A. Mansouri, "Shielding characteristics of nanocomposites for protection against X-and gamma rays in medical applications: Effect of particle size, photon energy and nano-particle concentration," Radiat. Environ. Biophys., 1−8 (2020).
https://doi.org/10.1007/s00411-020-00865-832780196

32. S. Malekie, F. Ziaie, S. Feizi, and A. Esmaeli, "Dosimetry characteristics of HDPE−SWCNT nanocomposite for real time application," Nucl. Instrum. Methods Phys. Res., Sect. A **833**, 127−33 (2016).
https://doi.org/10.1016/j.nima.2016.07.017

33. K. K. Sadasivuni, A. Saiter, N. Gautier, S. Thomas, and Y. Grohens, "Effect of molecular interactions on the performance of poly (isobutylene-co-isoprene)/graphene and clay nanocomposites," Colloid Polym. Sci. **291**, 1729−40 (2013).
https://doi.org/10.1007/s00396-013-2908-y

34. Y. Wang, J. Ye, and W. Tian, "Shape memory polymer composites of poly (styrene-b-butadiene-b-styrene) copolymer/liner low density polyethylene/Fe_3O_4 nanoparticles for remote activation," Appl. Sci. **6** (11),

333 (2016).
https://doi.org/10.3390/app6110333

35. I. M. Low and N. Z. Azman, *Polymer Composites and Nanocomposites for X-Rays Shielding* (Singapore, Springer, 2020).

36. S. Malekie and N. Hajiloo, "Comparative study of micro and nano size WO3/E44 epoxy composite as gamma radiation shielding using MCNP and experiment," Chin. Phys. Lett. **34**, 108102 (2017).
https://doi.org/10.1088/0256-307X/34/10/108102

37. F. Kazemi, S. Malekie, and M. A. Hosseini, "A Monte Carlo study on the shielding properties of a novel polyvinyl alcohol (PVA)/WO3 composite, against gamma rays, using the MCNPX code," J. Biomed. Phys. Eng. **9**, 465 (2019).
https://doi.org/10.31661/jbpe.v0i0.111431531300

38. M. J. Berger, J. H. Hubbell, S. M. Seltzer, J. Chang, J. S. Coursey, R. Sukumar, D. S. Zucker, and K. Olsen, XCOM: Photon Cross Section Database, version 1.5 (Natl. Inst. Standards Technol., Gaithersburg, MD 2010). http://physics.nist.gov/xcom. Accessed October 3, 2020.

39. J. H. Hubbell and S. M. Seltzer, *Tables of X-Ray Mass Attenuation Coefficients and Mass Energy-Absorption Coefficients 1 keV to 20 MeV for Elements Z = 1 to 92 and 48 Additional Substances of Dosimetric Interest* (Natl. Inst. Standards Technol.-PL, Gaithersburg, MD, 1995).

40. J. M. Boone and A. E. Chavez, "Comparison of X-ray cross sections for diagnostic and therapeutic medical physics," Med. Phys. **23**, 1997−2005 (1996).
https://doi.org/10.1118/1.5978998994164

41. R. S. Niranjan, B. Rudraswamy, and N. Dhananjaya, "Effective atomic number, electron density and kerma of gamma radiation for oxides of lanthanides," Pramana **78**, 451−8 (2012).
https://doi.org/10.1007/s12043-011-0247-4

42. M. Büyükyıldız, "Calculation of effective atomic numbers and electron densities of different types of material for total photon interaction in the continuous energy region via different methods," Sakarya Univ. J. Sci. **21**, 314−23 (2017).
https://doi.org/10.16984/saufenbilder.283266

43. S. R. Manohara, S. M. Hanagodimath, K. S. Thind, and L. Gerward, "On the effective atomic number and electron density: A comprehensive set of formulas for all types of materials and energies above 1 keV," Nucl. Instrum. Methods Phys. Res., Sect. B **266**, 3906−12 (2008).
https://doi.org/10.1016/j.nimb.2008.06.034

44. B. Akça and S. Z. Erzeneoğlu, "The mass attenuation coefficients, electronic, atomic, and molecular cross sections, effective atomic numbers, and electron densities for compounds of some biomedically important elements at 59.5 keV," Sci. Technol. Nucl. Install. **2014**, 901465 (2014).
https://doi.org/10.1155/2014/901465

45. M. L. Taylor, R. L. Smith, F. Dossing, and R. D. Franich, "Robust calculation of effective atomic numbers: The Auto-Zeff software," Med. Phys. **39**, 1769−78 (2012).
https://doi.org/10.1118/1.368981022482600

46. R. A. Novelline and L. F. Squire, *Squire's Fundamentals of Radiology,* 7th ed. (Harvard Univ. Press, Harvard, 2018).

47. S. Nambiar and J. T. Yeow, "Polymer-composite materials for radiation protection," ACS Appl. Mater. Interfaces **4**, 5717−26 (2012).
https://doi.org/10.1021/am300783d23009182

48. J. Wang, X. Duan, J. A. Christner, S. Leng, K. L. Grant, and C. H. McCollough, "Bismuth shielding, organ-based tube current modulation, and global reduction of tube current for dose reduction to the eye at head CT," Radiology **262**, 191−8 (2012).
https://doi.org/10.1148/radiol.1111047022190658